Next Energy 8 (2025) 100335

Contents lists available at ScienceDirect

Next Energy

journal homepage: www.sciencedirect.com/journal/next-energy

Research article

Investigating the impact of preparation routes on the properties of copper-decorated silicon particles as anode materials for lithium-ion batteries☆

Khryslyn G. Araño[a,*], Beth L. Armstrong[b], Anton W. Tomich[c], Matthew S. Chambers[a], Joseph Quinn[d], Harry M. Meyer III[a], Chanaka Kumara[b], Zoey Huey[e], Chun-Sheng Jiang[e], Chongmin Wang[c], Christopher S. Johnson[c], Raymond R. Unocic[f], Gabriel M. Veith[a,*]

[a] Chemical Sciences Division, Oak Ridge National Laboratory, Oak Ridge, TN 37831, United States
[b] Materials Science and Technology Division, Oak Ridge National Laboratory, Oak Ridge, TN 37831, United States
[c] Chemical Science and Engineering Division, Argonne National Laboratory, Argonne, IL 60439, United States
[d] Environmental Molecular Sciences Laboratory, Pacific Northwest National Laboratory, Richland, WA 99354, United States
[e] Materials Science Center, National Renewable Energy Laboratory, Golden, CO 80401, United States
[f] Department of Materials Science and Engineering, North Carolina State University, Raleigh, NC 27606, United States

ARTICLE INFO

Keywords:
Silicon anode
Lithium-ion batteries
Milling
Physical vapor deposition
Sputtering
Metal coating

ABSTRACT

In recent years, the calendar life of Si has been recognized as a significant issue that must be addressed prior to technology deployment: The carbon conductive additive is a potential source of parasitic side reactions. However, carbon remains essential due to the low electronic conductivity of Si. In this study, we investigate the use of Cu as a conductive additive and potential alternative to carbon. Some Cu-decorated silicon particles (Si^{Cu}) were prepared using physical vapor deposition (PVD) via sputtering and high-energy milling. Other Si^{Cu} particles were prepared by using a solution method and examined briefly. The milling method caused Cu to appear as island-like features on the Si surface, whereas the PVD method initially produced similar island-like features that gradually developed into a continuous coating around the Si as sputtering time increased. Electrodes fabricated from Si^{Cu} exhibited lower overall resistivity, demonstrating the beneficial effect of Cu in improving electronic percolation through the electrode. Electrochemical tests showed that the milled Si^{Cu} exhibited higher capacity retention, improved rate capability, and lower overpotential. Furthermore, Si^{Cu} coupled with an NMC811 cathode exhibited lower leakage currents compared with the baseline silicon, indicating that incorporating Cu provided an additional advantage of minimizing parasitic currents in the cells.

1. Introduction

Silicon has emerged as a promising anode material for high-energy-density Li-ion batteries because of its high theoretical gravimetric capacity, equivalent to 3579 mAh g^{-1} for the formation of $Li_{15}Si_4$ alloy at room temperature [1]. To enhance the performance of Si, various strategies, including the development of porous architectures and electrolyte studies, have been explored [2–5]. Despite these advances, Si-based electrodes still typically require a minimum of 10% conductive additives to overcome their inherently low electronic conductivity and to ensure effective electronic contacts within the electrode. Moreover, even with sufficient carbon concentration, the typical carbon black additives tend to agglomerate [6], decreasing their ability to create an electronically percolating network throughout the electrode, besides also contributing to irreversible capacity losses [7,8]. Furthermore, carbon was found to affect both homogeneity and percolation. In our prior investigation [6], we determined that the concentration of carbon influences the uniformity of the electrode produced. Specifically, a 10% concentration of carbon conductive additive was deemed optimal compared with concentrations of 5% and 2%, facilitating the even dispersion of Si and carbon black within the electrode. However, higher concentrations of carbon also correlate with increased parasitic side

* Corresponding authors.
E-mail addresses: khryslyn.arano@gmail.com (K.G. Araño), veithgm@ornl.gov (G.M. Veith).

https://doi.org/10.1016/j.nxener.2025.100335
Received 25 November 2024; Received in revised form 20 May 2025; Accepted 26 May 2025

reactions [6] and electrolyte decomposition [9] that can exacerbate calendar life issues associated with Si anodes.

An alternative approach to enhancing the conductivity of Si-containing electrodes involves employing carbon coating [2,10], which others claim to simultaneously address the challenges associated with Si cycling, notably severe volume expansion (~300%) [11]. Researchers have also incorporated metals, specifically Cu and Ag, into Si electrodes because of their high electrical conductivity [12–19]. Metal coatings, or decorations, on Si particles have been prepared mostly from solution via electroless deposition in order to individually coat the Si particles. For instance, Ag-coated Si particles are typically prepared using $AgNO_3$ [13,14,18], whereas Cu-coated particles are prepared from $CuSO_4$ [12]. Magnetron sputtering has also been applied to deposit Cu on top of Si thin films, creating another architecture in which an entire film of Si is capped with a layer of Cu [17]. In another study [20], porous Cu/Si electrodes have been prepared, although Cu primarily functions as the current collector rather than as an additive. Metals, including Cu, Ag, and Ni, have also been introduced as coatings onto graphite anodes for Li-ion batteries [21–24]. Generally, improved rate behavior and discharge capacities are observed; these qualities are attributed to reduced charge transfer and solid electrolyte interface (SEI) resistance. In particular, Cu [21] or Cu_2O [23] can suppress electrolyte decomposition at the anode interface. Moreover, Sandu et al. [22] highlight the significance of metal concentration, noting that higher concentrations, such as 33% and 43%, can impede Li diffusion into the active material.

In this study, we explore the potential of replacing conductive carbon materials with metallic Cu as a proof of concept. Although the incorporation of Cu may introduce additional costs to electrode preparation, it offers significant advantages, including faster charging capabilities and enhanced interfacial stability. These improvements open up new avenues in materials development, with potential benefits for fast-charging applications and extended calendar life. Prior work has demonstrated that high-energy milling reproducibly yields Si particles in the micrometer and submicrometer range—a near prerequisite for Si-based anodes [25]. Additionally, we have demonstrated surface functionalization of Si for improved processing and performance using this mechanochemical approach [6,25]. Instead of sputtering directly on top of the electrode, we apply high-energy ball milling and physical vapor deposition (PVD) via sputtering to individually decorate or coat the Si particles with Cu, obtaining Si^{Cu}. Furthermore, we briefly investigate a solution method as an alternative synthesis route. Focusing on the milling and PVD methods, we explore how these 2 preparation techniques influence the physicochemical properties of Si powders and their electrochemical performance in half cells. The presence of these conductive particles on the Si surface is expected to enhance electronic conductivity within the electrode, potentially permitting the reduction of carbon additive concentration in the electrode formulation. This work underscores the viability of preparing Cu-decorated Si powders, particularly via high-energy milling, which allows for potential upscaling. Our approach leads to unique microarchitectures and phases that can be effectively transformed into battery electrodes using traditional fabrication techniques such as tape casting. Notably, this method also enhances rate performance, reduces overvoltage, and minimizes losses.

2. Experimental section

2.1. Preparation of Si^{Cu} powders

The Si^{Cu} materials were prepared by 3 methods: a mechanochemical approach, a PVD method, and a solution synthesis. The 3 processes started with intrinsic Si boules (El-Cat). The boules were cleaned using successive washes of hot acetone, methanol, and a 3:1 ratio of NH_4OH/H_2O_2 (reagent-grade chemicals, Fisher), followed by a 2 min dip into a 5% HF solution prepared with 18 MΩ deionized water, and a final deionized water wash before drying in air. The cleaned boule was pulverized in a rock crusher into a < 18 mesh powder [26].

For the PVD-grown Si^{Cu}, the < 18 mesh Si powder was loaded in air in a 125 mL stainless steel mill jar with 3/32 in. 440C milling media (Union Process) and propylene carbonate (Aldrich 99.7%) with a mass ratio of Si to media to propylene carbonate of 7:52:8. The material was milled in a Retsch eMax mill for 6 milling cycles of 8 min on/20 min off. The temperature was limited to 60 °C during the milling. The propylene carbonate was used to passivate the Si surface and prevent or minimize the rejoining of the cleaved Si during milling. The slurry-like material was dried at 250 °C for 2 h to remove excess propylene carbonate, resulting in the Si powder. The Si powder was placed in a 12 cm diameter Al weighing dish (~10 g), which was loaded onto a stereo speaker in a vacuum deposition chamber. The speaker was connected to classic 1980s heavy metal music, which generates a random set of vibrations, causing the powder to fluidize and tumble [27–32]. Located 5 cm above the speaker/powder bed was a 2 in. diameter magnetron sputtering source with a 2 in. diameter Cu target (99.999% pure). The chamber was evacuated to a pressure of less than 2×10^{-6} Torr. For the deposition, a small amount of Ar (99.9995%; Airgas) was dosed into the chamber at 20 SCCM, and the pressure was increased to 16 mTorr. The Cu was sputtered at an applied power of 50 W, generating atomic Cu species that deposited onto the Si powder, forming the PVD-grown Si^{Cu} materials. Increasing the deposition time resulted in more Cu deposition onto the exterior surface of the fluidized powders. Samples were deposited for 1 h 4 min, 3 h 27 min, and 7 h 45 min and used without further processing.

The PVD-grown Si^{Cu} samples were evaluated using inductively coupled plasma optical emission spectroscopy (ICP-OES; Thermo Scientific iCAP 7400 ICP-OES Duo) to quantitatively characterize the Cu:Si ratio. Samples were prepared by dissolving approximately 0.05 g of material in a mixture of 4 mL of HNO_3 (Fisher Chemical, trace metal grade) to oxidize the Si nanoparticles and approximately 0.5 mL of 5% HF (diluted from concentrated HF solution; Sigma Aldrich, Trace metal). The dissolution was allowed to complete for 24 h. The final mixture was diluted with 18 MΩ deionized water. Unreacted HF was observed to skew the silicon signal from etching the glass nebulizer of the HF. The error was estimated to increase the silicon content by 0.1 ppm, which was accounted for in the data analysis.

For the milled Si^{Cu} materials, the same < 18 mesh Si powder was mixed with Cu powder (Alfa Aesar; −170 + 400 mesh) along with the same 3/32 in. 440C milling media and propylene carbonate. The amount of Cu was equivalent to the volume needed to match the volume of 10 wt % C45 carbon black typically used in a battery electrode formulation. For these experiments, 36 g of Si was mixed with 20 g of Cu along with 248 g of milling media and 43 g of propylene carbonate. The material was milled in a Retsch eMax mill for 6 milling cycles of 8 min on/20 min off. The temperature was limited to 60 °C during the milling. The slurry-like material was dried at 250 °C for 2 h to remove excess propylene carbonate, resulting in the free-flowing Si^{Cu} powder. Finally, a nondecorated baseline Si material was also prepared for comparison [6].

For the third method, Si^{Cu} (1%, 2%, and 5% w/w Cu) was prepared by dropwise addition of an aqueous 0.1 mol/L copper(II) formate dihydrate solution (0.0526 g, 5% Cu) to a suspension of 1.0 g of the baseline Si in 50 mL H_2O. Upon complete addition of the copper(II) formate dihydrate solution, the suspension was allowed to stir for 2 h at 70 °C to ensure homogeneity. The solution was then heated at 120 °C to dryness, yielding a fine, dark brown powder. The copper(II) formate dihydrate–doped Si powder was placed in an alumina crucible (McMaster-Carr) and heated in a sealed furnace (Lindberg/Blue M) to 450 °C at a ramp rate of 3 °C/min for 12 h under a 2.5% H_2/Ar gas flow. The powder was stored in an Ar-filled glovebox before its use in electrode fabrication.

2.2. Zeta potential and particle size measurements

The zeta potential and particle size of the baseline Si and Si^{Cu} were measured using NanoBrook 90Plus PALS from Brookhaven Instruments. Each Si powder sample was dispersed in N-methyl-2-pyrrolidone (NMP)

solvent. The concentrations of the dispersions are reported in our prior research [6,10,25]. Phase analysis light scattering (PALS) mode and dynamic light scattering (DLS) were employed to determine the zeta potential and the particle size, respectively. The reported values for each measurement are the average of 100 measurements.

2.3. X-ray photoelectron spectroscopy

A Specs EnviroESCA spectrometer was used for X-ray photoelectron spectroscopy (XPS) measurements of the Si powders. The spectrometer was operated at 15 kV with an Al Kα monochromatic source (1486.6 eV). The Si powders were introduced into the XPS chamber under ambient conditions. Survey scans were obtained using 100 eV pass energy and a step energy of 1 eV; high-resolution scans were performed using 50 eV pass energy and a step energy of 0.1 eV. To correct for charging, all spectra were calibrated against the carbon 1 s peak at 284.5 eV. Data were analyzed using the SpecsLab Prodigy software from SPECS [6].

XPS analysis of the cycled electrodes was performed using a Thermo Scientific (Waltham, Massachusetts, USA) Model K-Alpha instrument, which uses monochromatic and microfocused Al Kα X-rays (1486.6 eV). To prevent air exposure, the samples were prepared inside an Ar-filled glovebox and then transferred to the XPS instrument using a vacuum transfer holder. A 400 μm X-ray spot size was used for sample analysis to maximize signal strength and achieve an average surface composition over the largest possible area. Survey spectra were acquired using a pass energy of 200 eV; high-resolution core-level spectra were obtained using a pass energy of 50 eV. Throughout the data collection process, the charge-neutralization flood gun was employed to maintain stable analysis conditions. Data acquisition and processing were performed using the Thermo Scientific Advantage XPS software package (v.5.96), incorporating mixed Gaussian/Lorentzian peak shapes and a Shirley/Smart-type background model for peak fitting.

2.4. Scanning transmission electron microscopy

Cryo-scanning transmission electron microscopy (STEM) was performed on a 300 kV monochromated FEI Titan TEM with a probe aberration corrector. Electron energy loss spectroscopy (EELS) was performed on a Gatan Image Filter (GIF)—Quantum spectrometer. The dwell time was 20–50 ms, the dispersion was 0.05 eV/ch, and the pixel width was ~2.5–3.5 nm. The Cu $M_{2,3}$-edge was analyzed with a Hartree-Slater cross-section model, and the Si-$L_{2,3}$-edge was analyzed with Si and SiO_2 standards as the cross-sectional model. All spectra were corrected for plural scattering. EDS elemental mapping was performed with an Oxford Instruments AZTEC X-Max detector.

STEM-EDS analysis of the solution-prepared Si^{Cu} was performed using a Thermo Fisher Scientific Titan STEM, which is equipped with a Super-X EDS system and operated at 200 kV.

2.5. X-ray diffraction and Rietveld analysis

Powder X-ray diffraction (XRD) data were collected on milled Si^{Cu} and PVD-grown Si^{Cu} samples using a Rigaku SmartLab in Bragg Brentano geometry with a HyPix detector. Data were collected using a Cu source with a 2:1 $Kα_1$:$Kα_2$ ratio ($λ_1$ = 1.54056 Å; $λ_2$ = 1.54439 Å), a θ/2θ range of 10°–90°, a step size of 0.01°, and a scan rate of 1.5° min^{-1}.

Rietveld analysis [33] was performed using TOPAS Academic v7 [34] in order to determine phase purity. Four phases were included in the analysis: Si (starting model: Többens et al. [35]), Cu (starting model: Shkvarina et al. [36]), Cu_2O (starting model: Foo et al. [37]), and Cu_3Si (starting model: Dodony et al. [38]). A 12-fold Chebyshev polynomial was used to model the background, and a single pseudo-Voigt Thompson–Hastings–Cox function was applied to all samples to model peak shapes. The cell parameters of each phase were refined with symmetry constraints. A single atomic displacement parameter was used for all sites in each individual phase. For the analysis of the Si^{Cu}-milled sample, a double-Voigt function [39] was included to model the size-broadening effect on the peaks arising from Cu_2O. This function uses the Scherrer equation, (1), to determine the volume-weighted mean column height, L_{vol}:

$$\beta = \frac{k\lambda}{L_{vol}\cos\theta} \tag{1}$$

where β is the full width at half-maximum, k is the Scherrer constant (0.89 for cubic systems,), λ is the wavelength of the diffracted radiation, and θ is the Bragg angle. Additionally, the Stokes and Wilson-modified Scherrer equation, (2), was used as follows:

$$\beta_i = \frac{\lambda}{L_{vol}\cos\theta} \tag{2}$$

where β_i are the integral breadths and $k = 1$. This function was used to determine the Si and Cu crystallite sizes, but this attempt resulted in large errors. Instead, the single-peak approach (SPA), where a pseudo-Voigt function was fitted against the (1 1 1) reflection of Si and Cu, was used to determine the FWHM. The SPA used a Scherrer constant of $k = 1$ and a weighted-mean value of λ = 1.54185 Å. In addition, because the (2 0 0) reflection from Cu_2O overlaps with the Cu (1 1 1) reflection in the milled sample and the contribution from Cu is small in the sputtered sample, the SPA was performed against the Rietveld-calculated pattern arising from Cu as outputted by TOPAS.

2.6. Electrode fabrication

Slurries were prepared using the Si powder (Si or Si^{Cu}), P84 polyimide (Ensinger Austria) binder, and C45 carbon black (TIMCAL Super C45) as a conductive additive. The slurry components were loaded in a 20 mL polyethylene bottle with 5 pieces of 5 mm beads of yttria-stabilized zirconia as milling media. Milling was then performed using a Turbula mixer for 1 h. The slurry was cast on a 9 μm Cu foil substrate (battery grade) with a 100 μm film applicator. A Si:binder:conductive additive with a mass ratio of 80:10:10 was prepared. The electrodes were dried at 100 °C to remove the NMP solvent and moisture, followed by a curing step at 350 °C at 1 h under an Ar atmosphere using a ramp rate of 10 °C/min [6,10,25]. For the solution-prepared Si^{Cu} particles, electrodes were prepared by using the same formulation as the milled and PVD-grown samples, but the coating was performed using a 50 μm wet gap. The resulting active loading is 0.8–0.9 mg cm^{-2}. The electrodes were allowed to dry at 75 °C for 1 h. Then they were transferred to a vacuum oven where they were dried for at least 12 h at 80 °C. A punch (Nogami) was used to create Ø15 mm electrodes, which were then annealed at 300 °C under vacuum. Electrodes were subjected to an additional 2 h at 110 °C in a vacuum oven within an Ar-filled glovebox before use.

2.7. Scanning electron microscopy

The electrode cross-section morphology and element distribution analysis were performed using a Hitachi S-4800 scanning electron microscopy (SEM) instrument equipped with energy-dispersive spectroscopy (EDS). The EDS spectra were obtained using an acceleration voltage of 5 kV.

2.8. Scanning spreading resistance microscopy

Scanning spreading resistance microscopy (SSRM) [40,41] is based on the contact mode of atomic force microscopy (AFM): a bias voltage is applied between the probe and sample, and the current through the probe is measured. This technique maps the local resistance beneath the probe in a volume of a hemisphere with a radius of about 50 nm. The AFM (Bruker Dimension Icon and Nanoscope V controller) is set up in an Ar-filled glovebox, and a logarithm scale current amplifier (Bruker SSRM module) with a wide resistance range of about 10^3 to 10^{14} Ω was

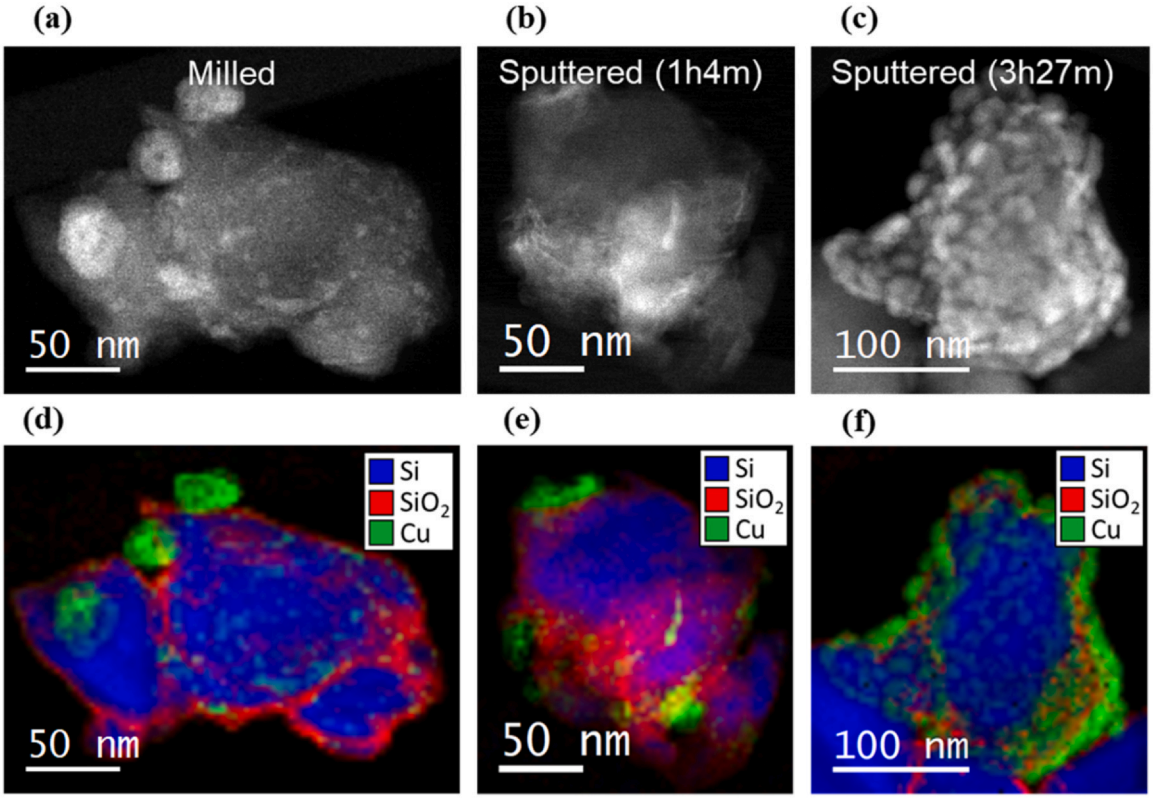

Fig. 1. STEM images of (a) Milled Si^{Cu}, (b) sputtered Si^{Cu} (1 h 4 m), and (c) sputtered Si^{Cu} (3 h 27 m) particles; (d–f) corresponding EELS maps of the of the various samples (blue corresponds to Si, red to SiO_2, and green to Cu).

used for resistance measurement. A bias voltage was applied to the sample, and the probe (diamond-coated Si probe, Bruker DDESP-V2) was floating grounded. The measured resistance is the sum along the current route. The resistance at the back contact is much smaller than the measured resistance (i.e., not a contributing factor). The probe/sample contact resistance is minimized by pressing the probe into the sample with a relatively large contact force of about 1 mN, so the measured resistance is dominated by the sample's spreading resistance.

2.9. Electrochemical testing

Half cells were assembled using coin cells (R2032) in an Ar-filled glovebox. The 13 mm diameter Si disks were used as working electrodes, and 14 mm diameter Li metal disks (0.75 mm thickness, Alfa Aesar) were used as counter/reference electrodes. Celgard 2325, with a diameter of 19 mm, was used as the separator. The electrolyte was 1.2 mol/L $LiPF_6$ solution in ethylene carbonate and ethyl methyl carbonate (3:7 by weight), denoted as Gen2, with 3 wt% fluoroethylene carbonate (FEC). After assembly, a resting period of 4 h was observed before cycling. Cycling was performed in galvanostatic mode using a BioLogic potentiostat at room temperature with voltage cutoffs from 50 mV to 1 V. The formation step was performed at C/20, followed by long-term cycling at C/3. In this study, 1 C is defined based on the formation of the $Li_{15}Si_4$ alloy or a theoretical capacity of 3579 mAh g^{-1}.

Leakage current tests were conducted using a full-cell configuration. The full cells were assembled using either a nonprelithiated baseline Si or nonprelithiated Si^{Cu}, matched with $LiNi_{0.8}Mn_{0.1}Co_{0.1}O_2$ (NMC811) with an areal loading of 4.0 mAh cm^{-2} obtained from the Cell Analysis, Modeling, and Prototyping (CAMP) facility at Argonne National Laboratory. The cathodes were dried at 90 °C overnight under vacuum and then transferred into an Ar-filled glovebox for coin cell assembly. Gen2 + 3 wt% FEC electrolyte was used, and Celgard 2325 served as a separator. Before the leakage current measurements, the cells underwent 3 formation cycles between 3.0 V and 4.1 V at C/10. The cells were then charged again to 4.1 V and left for 180 h while the current was recorded. The reported leakage currents were normalized with capacity to allow comparison between systems.

3. Results and discussion

The Si^{Cu} powders were prepared by employing both a mechanochemical approach, a solutions-based process, and PVD technique, resulting in distinct architectures of Si particles decorated with Cu. The mechanochemical method involved high-energy ball milling of Si with Cu particles, whereas the PVD technique entailed sputtering of Cu from a target onto a tumbling dish containing the Si particles, leading to atomic deposition of Cu. The solution process involved the precipitation of copper on the silicon surface, followed by reduction to Cu°. Compared with electroless deposition or chemical reduction processes previously employed for metal coating on Si [12–14,18], high-energy ball milling offers the potential advantage of further reducing the size of Si particles while incorporating metal particles within and onto their surface, eliminating the need for additional steps such as precursor removal via washing or annealing. Similarly, the PVD process offers a potential advantage: Metal deposition occurs atom by atom onto Si, removing the necessity for further processing and allowing control over deposition thickness by adjusting the deposition time.

In terms of resulting architecture, Fig. 1 presents scanning transmission electron microscopy (STEM) and STEM/electron energy loss spectroscopy images, showing detailed structures of the Si particles subjected to either milling or sputtering with Cu. The Cu appears as bright spots due to the higher electron density. The Si particles exhibit irregular shapes, a consequence of the milling process employed to produce the baseline Si material. The energy-dispersive X-ray spectrometry (EDX) data revealed SiO_2 on the Si surface. In general, the electroless deposition technique has demonstrated uniform coverage of metal on Si powders [12,13,16]. Representative STEM data for 1, 2, and

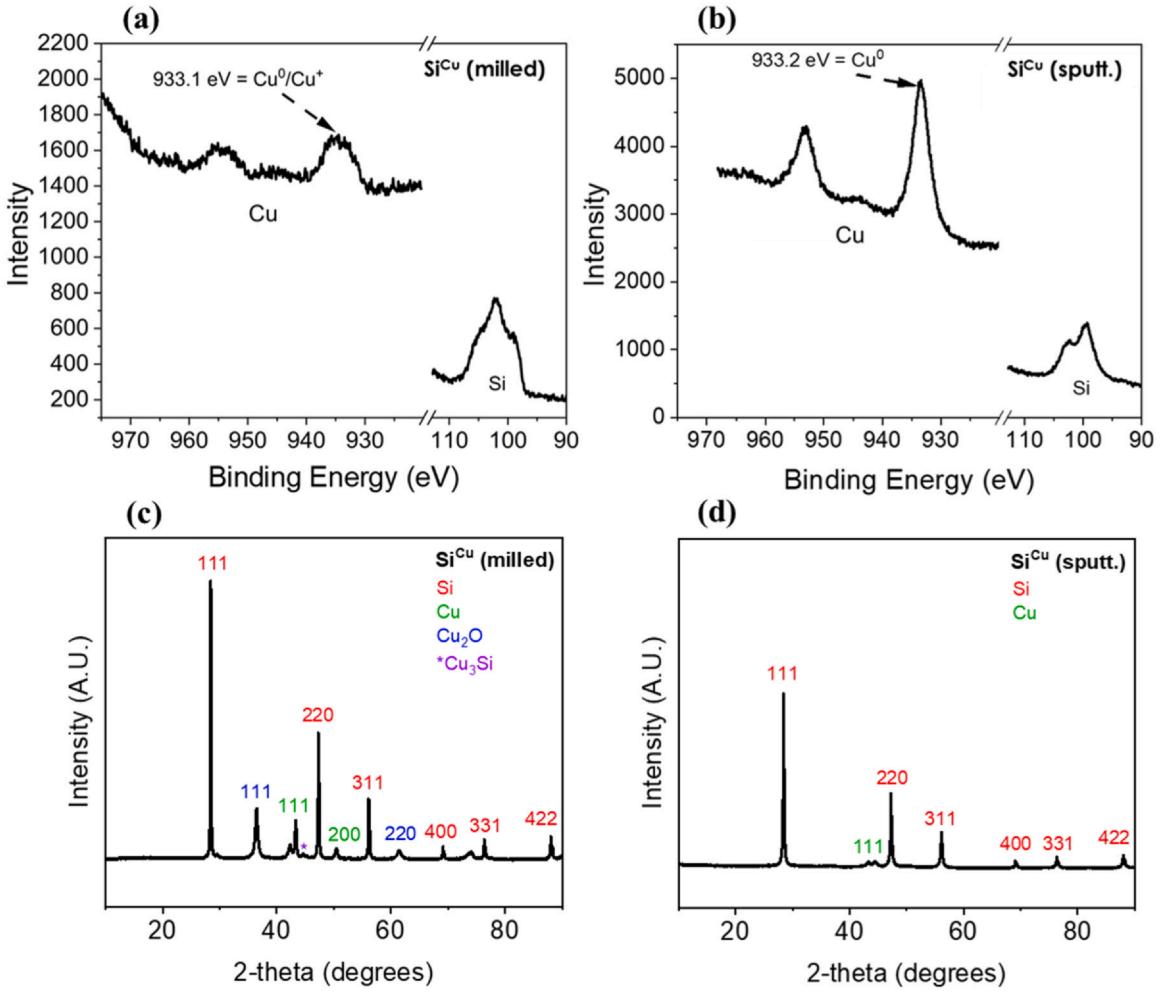

Fig. 2. XPS Cu 2p and Si 2p spectra of various samples: (a) Si^{Cu} (milled) and (b) Si^{Cu} (sputtered 7 h 45 m) powders. XRD patterns of other samples: (c) Si^{Cu} (milled) and (d) Si^{Cu} (sputtered 3 h 27 m). *The XPS Si 2p fits are shown in* Fig. S3.

5 wt% Cu from the sol–gel process are presented in Figs. S1a, S1b, and S1c. The data show homogeneous dispersed copper across the surface of the silicon materials. There is no evidence for the formation of discrete copper nanoparticles over atomically dispersed copper atoms. As opposed to electroless deposition, the high-energy milling process employed in this work resulted in a more random decoration of the Si, wherein the Cu particles exhibit an island-like distribution on the Si surface. Nonetheless, this sparse and random decoration is compensated by the uniform overall distribution of Si^{Cu} in the electrode, as discussed later. The PVD method facilitates a more consistent deposition of metals onto the Si surface; its uniformity varies based on sputtering duration. For instance, after 1 h 4 min of sputtering, the Si^{Cu} sample exhibits a surface structure similar to that obtained by Si^{Cu} milling, featuring Cu particles that form islands across the Si surface. In the milled sample, these Cu islands measure approximately 20–30 nm for larger particles. Numerous extremely small Cu particles, less than 5 nm in size, are also present. By contrast, the 1 h 4 m sputtered sample showcases Cu particles with more irregular shapes and sizes, ranging from less than 5 nm to around 20 nm. Notably, with extended sputtering durations, such as the 3 h 27 m sample shown in Fig. 1(c) and (f), Cu concentration increases noticeably, resulting in near-complete coverage of the Si surface by Cu. The Si^{Cu} 7 h 45 m sample is expected to exhibit even greater Cu coverage on the Si particles.

The presence of Cu on Si was also confirmed via XPS. Fig. 2a shows the metallic Cu signal at 933.1 eV for the milled sample. Fits to the Cu data are presented in Fig. S4. Notably, the broadened peak and the lack of satellite peaks are a possible indication of the presence of Cu_2O in addition to the metallic Cu. This is consistent with 2 species in the Cu XPS fits with peak splitting of 19.7 and 20.1 eV attributed to Cu^0 and Cu^{1+}. The signal also exhibits a weak intensity with a low signal-to-noise ratio, in agreement with the minimal presence of Cu dotting the Si surface, as observed in the STEM images in Fig. 1. For the sputtered samples, analysis was conducted on the Si^{Cu} 7 h 45 m particles, revealing a more pronounced metallic Cu peak at 933.2 eV. The stronger signal for Si^{Cu} 7 h 45 m aligns with the anticipated higher Cu content with longer sputtering time. For both the milled and sputtered powders, the visible Si signal around 100 eV indicates nonuniform Cu decoration or coating, exposing portions of the Si particles. The precipitation approach produced materials with XPS signals similar to PVD-grown copper and consistent with metallic Cu nanoparticles (Fig. S4). Moreover, the presence of the Si signal indicates that the coating thickness is less than 10 nm, considering the surface sensitivity of the XPS technique.

XRD analysis confirmed the presence of Cu_2O alongside the metallic Cu signal observed via XPS in the milled Si^{Cu} sample. Rietveld refinements were performed to ascertain the phase composition. The baseline sample (Fig. S2) exhibits an unaccounted peak at $2\theta \approx 44.5^{\circ}$; all other peaks are accounted for using Si alone, achieving a fit of $R_{wp} = 8.750\%$, $\chi^2 = 2.763$. In the milled sample, the Rietveld-derived weight percentages are 64.0(2)% Si, 9.5(2)% Cu, 25.7(2)% Cu_2O and 0.87(9)% Cu_3Si. The weight percentage of Cu_2O may be overestimated because of the size-broadening function being applied to its peak shape. By contrast, the composition of the sputtered sample is 94.0(9)% Si, 4.8(8)% Cu and 1.2(5)% Cu_2O. A large proportion of Cu in the milled sample

Table 1
Particle size and zeta potential of the neat Si and the Si^{Cu} particles measured by DLS and PALS, respectively

Active material	Particle size (nm)	Zeta potential (mV)
Baseline Si	220[6]	−45.0[6]
Si^{Cu} (milled)	299	−44.5
Si^{Cu} (sputtered 1h4m)	248	−17.8
Si^{Cu} (sputtered 3h27m)	236	−20.4
Si^{Cu} (sputtered 7h45m)	247	−15.8

appears to have been oxidized to Cu^+, whereas the Cu metal in the sputtered sample remains mostly neutral. Although a small amount of Cu_2O is present, with a relatively large error, the (1 1 1) reflection at $2\theta \approx 36.5^\circ$ is visible. As expected, the milled sample contains a larger weight percentage of Cu compared with the sputtered sample. The absence of discernible Cu^+ in the XPS data indicates that Cu is in close contact with SiO_2, which then reacts to form the copper(I) oxide. Although Cu_2O is electrochemically active [42], it is not anticipated to contribute to the capacities observed in this work because the electrochemical signals for Cu_2O (> 1 V vs. Li/Li^+) are beyond the potential window in this study (50 mV–1 V).

Furthermore, the crystallite sizes for all 3 phases were determined and are given in Table S1. The milled Si has larger crystallites, 131(2) nm, than the Si in the sputtered sample, 101(2) nm. The Cu crystallites are also larger in the milled sample, 70.6(2) nm, than in the sputtered example, 37.19(15) nm, indicating that they are more crystalline. This result is expected because in the sputtered sample, Cu was deposited atom-by-atom, whereas the milled sample used crystalline Cu that is ground into smaller crystallites and particles. The crystallites of Cu_2O detected in the milled sample are very small, 14.6(4) nm, indicating that the phase is poorly crystalline. Because of its very small contribution, the crystallite sizes of Cu_2O in the sputtered sample were not determined. Overall, the findings from STEM and XPS are different to those from XRD because the first 2 techniques rely on a single area of the examined materials, in addition to the surface-only analysis provided by XPS. By contrast, XRD evaluates the bulk of the material, offering a broader understanding of the composition of the powders.

Table 1 shows that the milled Si^{Cu} particles exhibit larger average particle sizes, 299 ± 25 nm, than those of the baseline material, 220 ± 10 nm. This phenomenon can be attributed to 2 factors. First, extra material is present on the surface of Si, as observed in the STEM images, leading to an increase in particle size. Second, the physics of milling potentially changes with the presence of Cu. Given the malleable nature of metals, the presence of Cu may absorb some of the impact from the high-energy milling process, possibly hindering the effective breakdown of Si particles compared with milling without Cu. For the PVD-grown materials, the average particle sizes are 248 ± 4 nm, 236 ± 4 nm, and 247 ± 4 nm for sputtering durations of 1 h 4 m, 3 h 27 m, and 7 h 45 m, respectively. These values are effectively similar to those of the baseline material, suggesting that the thickness of the Cu coating on the Si surface is no more than 10–20 nm, given the size of the baseline Si particles.

Furthermore, the zeta potential of Si also changes with the addition of Cu on its surface, specifically the sputtered samples. As shown in Table 1, the zeta potential of the sputtered Si^{Cu} powders is reduced by at least half (in absolute value) compared with the baseline Si, whereas the milled Si^{Cu} exhibits a zeta potential comparable to that of the baseline material. The zeta potential results may be influenced by the oxidation state of Cu on the Si surface. For the milled samples, Cu primarily exists as oxides, whereas for the sputtered samples, Cu remains in its metallic form, as indicated by XRD analysis. These observations indicate that metal decoration of Si and the preparation method influence the fundamental physicochemical properties of Si. These properties could subsequently affect the science of electrode manufacturing as well as the electrode performance.

Although the decorated particles exhibit a decreased zeta potential, which typically leads to agglomeration in suspension or poor mixing with carbon black, surface and cross-sectional SEM images of the electrodes in Fig. 3 both demonstrate a uniformly dispersed distribution of electrode components. For instance, the Si elemental image (Fig. 3, top row) showcases an even distribution of the active material. Furthermore, despite their lower concentration, Cu particles (Fig. 3, center) in the Cu-decorated electrodes are well-interspersed within the Si matrix, as evidenced by the faint Cu signal throughout the electrode. This apparent uniform distribution of a conductive element within the electrode is expected to improve the overall electronic percolation

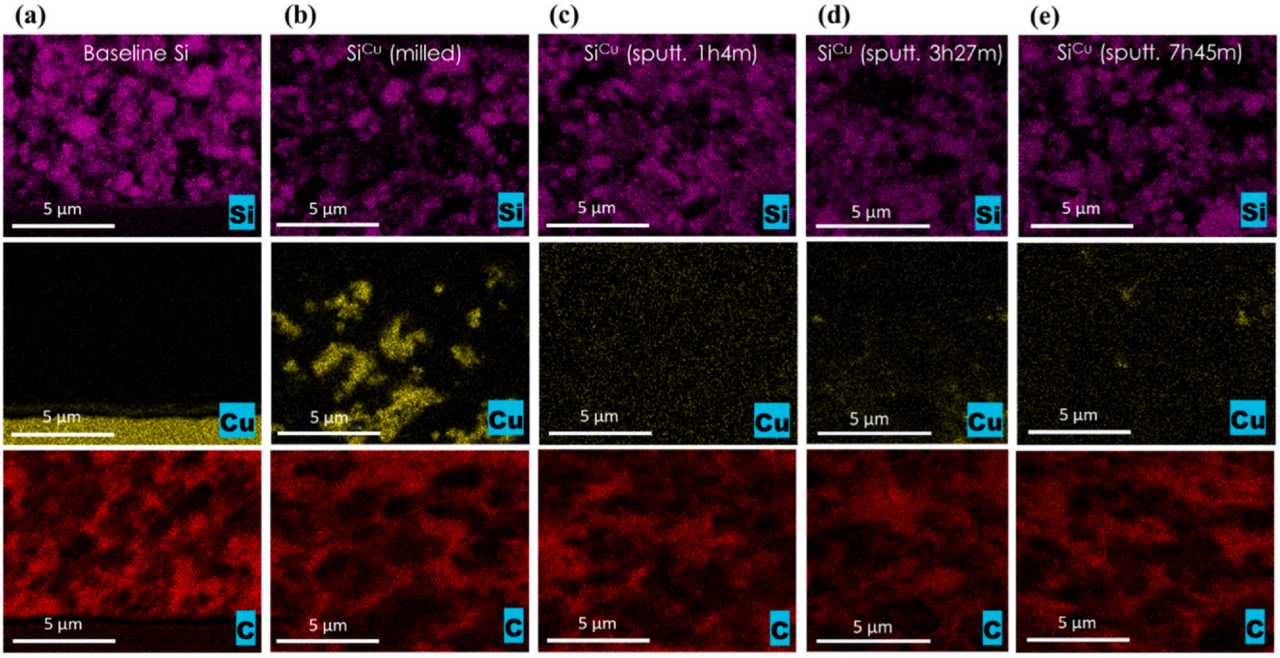

Fig. 3. Cross-sectional SEM-EDX images of the (a) baseline Si and Si^{Cu} prepared by (b) milling and sputtering methods: (c) 1 h 4 m, (d) 3 h 27 m, and (e) 7 h 45 m. *Note: The big pieces of Cu in (b) are contaminants from the current collector acquired during the preparation of the samples.*

within the electrode structure. Additionally, the elemental micrographs for carbon provide further confirmation of the effective dispersion of the conductive additive. Overall, these findings suggest that the electrode fabrication process successfully maintains a uniform distribution of components even after metal decoration. This capability is crucial for optimizing the electrode's performance.

The SSRM technique was used to examine the resistances of the cross-sectioned electrodes, offering insights into both their electrical characteristics and their topography. SSRM scans over the entire anode thickness, providing information on the resistivity distribution along the entire Si anode cross section. As shown in Fig. 4, which presents the SSRM images for both the baseline Si and the milled Si^{Cu} samples, brighter colors correspond to areas of lower resistivity, while darker colors indicate higher resistivity. The corresponding AFM images of the electrodes are shown in Fig. S5. The AFM images show that the Si^{Cu} electrode is more porous based on the examined cross-section. This observation aligns with the SEM images in Fig. 4, where the Cu-decorated particles appear qualitatively more porous than the baseline Si. To further confirm, additional AFM images were taken along with roughness and histograms of spanning range (height spans), as shown in Figs. S6–S9. Both roughness and spanning range of the Cu-decorated sample are significantly larger than that of the baseline material, possibly indicating that the Cu–Si electrode is more porous.

In general, the carbon black agglomerates display lower resistivity, and Si agglomerates demonstrate higher resistivity. Additionally, the electrodes exhibit numerous voids, indicating their porous nature. In the Si^{Cu} electrode, no lower-resistivity material was clearly observed on the edge of the Si particles. This result is unexpected, considering the conductivity of Cu and the presence of Cu particles on the Si surface according to the STEM images in Fig. 1. Two possibilities could explain this observation. First, the Cu particles are very small, about 5 nm in size, rendering them electrically isolated and disconnected from the conduction network. For low-resistivity materials measurable by SSRM, either small (nanometers) particles have electrical connection with the surrounding network, or the low-resistivity material has a size larger than around 50 nm. Second, the small metal/metal oxide particles may not possess high conductivity compared with the bulk metal. The former possibility seems plausible given the small scale of the Cu particles (a few nanometers). Nevertheless, the baseline Si electrode demonstrates higher overall resistivity, as indicated by the average resistance of 10.01 Log(Ω) compared with the Cu-decorated electrode with an average resistance of 9.41 Log(Ω). Moreover, these findings are consistent with the SEM observations in no distinct Cu particles were found along the electrode cross section. Regarding the second possibility, XRD analysis confirmed the notable presence of copper oxides, which inherently exhibit lower conductivity than their metallic counterparts.

Fig. 5(a)–(d) displays the half-cell charge–discharge voltage profiles of the baseline Si in comparison with the Si^{Cu} prepared via sputtering. Particularly noteworthy is the observed capacity increase beyond 20 cycles across all samples, which we attribute to the activation of the Si particles. Nonetheless, the electrodes start to behave as expected beyond 40 cycles, characterized by a gradual decline in capacity upon cycling. A noticeable advantage of Si^{Cu}, according to Fig. 5(a)–(d), is the improved cycling stability of the electrodes. Considering the phenomenon mentioned above, the capacity retention was assessed within the 40–100 cycle range. The neat Si exhibits the lowest retention at 51.2% after 100 cycles, whereas all the Si^{Cu}-based electrodes demonstrated higher stability during cycling, equivalent to 62.1% for Si^{Cu} 1 h 4 m, 57.1% for Si^{Cu} 3 h 27 m, and 58.9% for Si^{Cu} 7 h 25 m. However, although the presence of PVD Cu on the Si particles seems to benefit the cycling stability of Si, the lower specific capacities of these particles compared with the neat Si indicates a detrimental issue. For example, the baseline Si electrode delivers about 1000 mAh g_{Si}^{-1} long after the activation phase, typically occurring around 40 cycles. By contrast, the specific capacities show a decline upon metal decoration, and this decline is emphasized at longer sputtering durations. For instance, the 1 h 4 m and 3 h 27 m PVD-grown Si^{Cu} electrodes deliver approximately 700 mAh g_{Si}^{-1} after 40 cycles, and capacity drops to about 600 mAh g_{Si}^{-1} for the 7 h 45 m electrode. These lower specific capacities for Si^{Cu} can be attributed to 2 factors: (i) The specific capacities were normalized by the mass of Si with Cu; therefore, an additional electrochemically inactive mass of Cu was not taken into account when calculating for capacities. (ii) The conformal islands on the Si surface present an additional barrier for Li-ion transport [22]. The second case is supported by the STEM images presented in Fig. 1, wherein Cu covers almost the entire surface of some Si particles after approximately 3 h of sputtering. ICP-OES was performed on the PVD-prepared Si^{Cu} powders to determine the exact amount of Cu sputtered onto the powders and to ascertain whether accounting for the Cu mass would increase the specific capacities significantly. From Table S2, we confirm the increasing Cu content upon increase in sputtering time based on the mass ratio of Cu to Si (g_{Cu}/g_{Si}), which is equivalent to 0.015 for the 1 h 4 m sample, 0.052 for the 3 h 27 m sample, and 0.119 for the 7 h 45 m sample. Based on these ICP-OES results, the masses are comparable to the milled Si^{Cu} powders.

The half-cell charge–discharge performance of the milled Si^{Cu} was also evaluated, and results are presented in Fig. 5(e) and (f). Compared with the baseline Si in Fig. 5a, the capacity retention achieved by milled Si^{Cu} is notably superior, demonstrating a decent capacity retention of

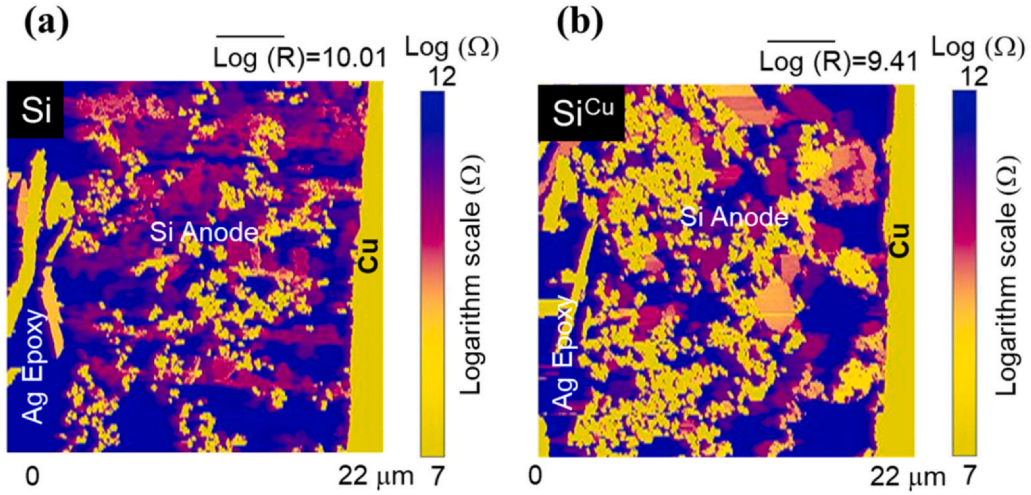

Fig. 4. SSRM resistance images acquired from (a) baseline Si and (b) Si^{Cu} (milled) electrode sample.

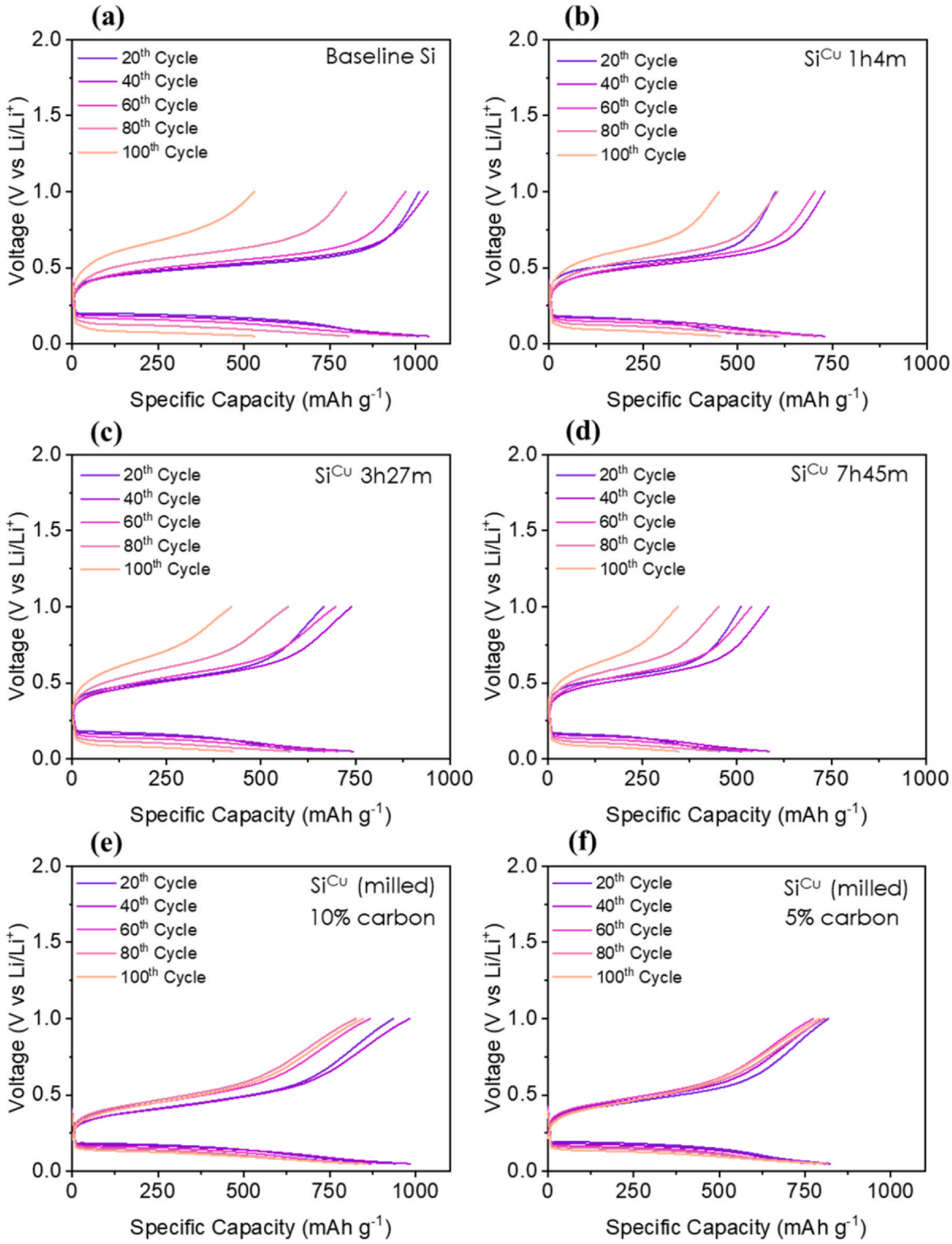

Fig. 5. Half-cell charge–discharge voltage profiles of the (a) baseline Si, (b) PVD-grown Si^{Cu} 1 h 4 m, (c) PVD Si^{Cu} 3 h 27 m, (d) PVD Si^{Cu} 7 h 45 m, (e) milled Si^{Cu} (10% C additive), and (f) milled Si^{Cu} (5% C additive) in Gen2 + 3 wt% FEC electrolyte at room temperature. A plot of specific capacity vs. cycle number with Coulombic efficiencies is presented in Fig. S10.

86.8% and maintaining a discharge capacity of 847 mAh g^{-1} after 100 cycles (Fig. 5e). By contrast, the baseline Si experiences a drop from a discharge capacity of 1038 mAh g^{-1} to 532 mAh g^{-1} after 100 cycles (Fig. 5a). Interestingly, despite the comparable masses of Si and Cu of the PVD-grown vs. the milled samples, the synthesis route significantly affects the performance, indicating that the method of Cu deposition onto the Si is critical. Specifically, the milled Si^{Cu} exhibits improved cyclability compared with the sputtered Si^{Cu} (Fig. 5[b]–[d]). The enhanced cycling stability of the milled Si^{Cu} may be linked to greater interfacial stability of the deposited Cu on Si during cycling. Prior work by Kim et al [12]. highlighted the interfacial stability of the Cu deposit on the cyclability of the cells. According to their work, Cu can detach from Si during cycling. This issue can be addressed by annealing the Cu-coated Si at 400 °C for 9 h, forming a Cu_3Si alloy that imparts interfacial

stability. In this study, the energy of milling could impart enough energy to drive the formation of a small, intermixed Si-Cu domains, as evident by the small concentration of Cu_3Si in the XRD pattern in Fig. 2c. These domains could promote the ion transport discussed above and the resulting overvoltage improvement.

A significant finding arising from the milled Si^{Cu} is its lower overpotential observed even during the early cycling stages, equivalent to approximately 0.3 V, in contrast to the sputtered and baseline electrodes, which exhibit an overpotential of about 0.4 V after 20 cycles. Importantly, the overpotential of the milled material remains constant upon continued lithiation and delithiation. However, the overpotential of the sputtered electrodes and the baseline material continue to evolve with cycling, ultimately reaching approximately 0.6 V after 100 cycles. Interestingly, the observed increase in overpotential occurs during the delithiation process, suggesting that the diffusivity of Li in Si during the alloying/dealloying processes or through the SEI is more favorable in the case of the milled Si^{Cu}, indicating a more efficient utilization of the electrode. Considering the SEM images indicated good dispersion of conductive Cu particles within the electrode, cells were constructed with a reduced C additive concentration in the Si anode (i.e., 5 wt%) to determine whether the cycling currents could be sustained by substituting carbon black with Cu. However, according to the specific capacities in Fig. 5f, a minimum of 10 wt% carbon seems to be required despite the addition of Cu particles onto Si. Specifically, approximately 300 mAh g^{-1} of capacity is lost because of the reduced carbon content. Nonetheless, an excellent capacity-retention equivalent to 98.5% is exhibited by the electrode containing 5 wt% carbon, potentially attributed to lower Si utilization and resulting in less stress/strain on the Si particles during cycling.

Based on the specific capacities obtained during cycling, particularly in the initial stages when the baseline Si and milled Si^{Cu} deliver approximately 1000 mAh g^{-1}, the decline in capacity noted with the baseline Si likely is not due to particle cracking, given the comparable or even lower Si utilization compared with the milled Si^{Cu}. Subsequently, the SEI composition of the Si electrodes was analyzed via XPS to determine whether the SEI affects the performance of the materials. From Fig. 6a, the carbon 1 s spectra indicate more carbonate-containing species in the baseline Si electrode, such as Li_2CO_3 and $C_4H_4Li_2O_6$ (LEDC), resulting from the reduction of the ethylene carbonate solvent [43], as evidenced by the more pronounced peak around 289.8 eV. Additionally, the baseline material also contains more C–O groups compared with Si^{Cu}. Meanwhile, Si^{Cu} has more C–C groups around 284.8 eV, indicating the presence of compounds such as CH_3CH_2OLi, resulting from ethyl methyl carbonate decomposition [43]. These findings align with the oxygen and carbon content from surface composition of the electrodes as detailed in Table S3. From the F 1 s spectra in Fig. 6b, the $LiPF_6$ salt in the electrolyte appears to decompose more readily in the case of Si^{Cu} to form LiF around 684.8 eV. Based on these results, the presence of Cu on the Si surface appears to alter the decomposition of the electrolyte, resulting in varying proportions of SEI species, particularly those containing carbon.

The carbon 1 s XPS spectra (Fig. 6d) of electrodes containing 5 wt % carbon exhibit similar characteristics to those with 10 wt% carbon, with more $–CO_3$ and C–O species observed in the baseline Si and more C–C groups for Si^{Cu}. Conversely, the fluorine 1 s XPS in Fig. 6e are very similar. Interestingly, the $Li_xPO_yF_z$ content based on phosphorous 2p spectra is consistently higher in electrodes that contain 5 wt% carbon (Fig. 6f), compared with those that contain 10% carbon (Fig. 6c). These electrodes contain more Li_xPF_y, indicating that the amount of carbon additive may also be changing the SEI. However, attributing the electrochemical behavior to phosphorus-containing SEI species proves challenging because the contribution of phosphorus comprises only about 2 atom % of the entire SEI. Thus, the cycling stability demonstrated by Si^{Cu} (5 wt% carbon) is likely due to the limited utilization of Si.

XRD profiles of the decorated powders in Fig. 2 show that the milled material possesses larger Si crystallite sizes equivalent to 131(2) nm, indicating a higher degree of crystallinity. However, prior research indicates that amorphous Si tends to show enhanced cyclability due to improved lithiation kinetics and favorable fracture behavior [44–47]. Therefore, despite changes in the crystallinity of the Si^{Cu} as influenced by the synthesis method, other factors seem to be primarily responsible for the enhanced performance of the milled samples compared with the sputtered materials. Although XPS analysis was not performed for the PVD-grown Si^{Cu}, the larger overpotential of the cells with sputtered Si^{Cu} in Fig. 5(b–d) compared to the cells with milled Si^{Cu} in Fig. 5(e) and (f) indicates that the passivation or SEI layers may be different. This conclusion agrees with the diameters of the semicircles in the Nyquist plots in Fig. 7, which are attributed to the interphase affecting the SEI and charge-transfer resistance. The charge-transfer process involves the desolvation of Li ions in the electrolyte, followed by diffusion through the SEI before the electrochemical reaction takes place [48]. The resistance associated with this process is typically influenced by factors such as battery aging and the evolution of the SEI during cycling. In Fig. 7, the observed increase in charge-transfer resistance upon cycling can be attributed to such phenomena.

The total internal resistance of the cells at approximately 100 kHz is similar for the milled and the sputtered samples, further supporting the SEM images showing homogeneously distributed Cu (on Si) throughout the electrode in both materials. Furthermore, the addition of Cu in the anode seems to contribute to the preservation of the overall internal cell resistance during cycling. In the case of the baseline Si, its high-frequency (~100 kHz) impedance steadily increases upon cycling, from around 10 Ω to around 17.5 Ω. This result may explain, at least partly, the increasing overpotential of the cell during cycling as shown in Fig. 5a. In the milled and sputtered Si^{Cu}, this high-frequency (~100 kHz) impedance remains relatively constant, increasing by approximately 3 Ω from 20th to 100th cycle, although the differences in performance for these decorated particles may arise more from the interphase, as mentioned previously. Moreover, the Warburg region at lower frequencies differs significantly among the 3 materials investigated. The Warburg feature of the milled Si^{Cu} is notably steeper than that of the baseline Si and sputtered Si^{Cu}. These significant differences in the Nyquist plot suggest that metal decoration of Si alters certain phenomena. In particular, diffusion within the porous electrodes [49] appears to be significantly modified with milled Si^{Cu}. The variations in impedance slopes in this region can be attributed to geometric effects, specifically the shape of the pores [50].

The half-cell rate performance of the baseline Si and milled Si^{Cu} was briefly assessed. As depicted in Fig. 8a, the inclusion of Cu particles clearly facilitates accessing higher capacities across various current densities. For example, Si^{Cu} exceeds the capacity of the baseline Si by an average of 451 mAh g^{-1} at C/20. Moreover, the extent to which Si^{Cu} surpasses the baseline Si capacity increases with increasing C-rate, indicating that the presence of conductive Cu aids in sustaining more-demanding current densities. For instance, at C/10, Si^{Cu} exceeds the baseline by an average of 679 mAh g^{-1}. This capacity further increases to 782 mAh g^{-1} at C/5 and 834 mAh g^{-1} at C/3. This result can be attributed to the overall lower resistivity of the Si^{Cu} electrodes based on the SSRM measurements. Finally, the ability of the electrode to recover capacities is also significantly improved in the case of Si^{Cu}. Specifically, upon lowering of the C-rate to C/10, the decorated electrode can deliver an average of 1843 mAh g^{-1}, compared with 729 mAh g^{-1} for the baseline material, from an original C/10 capacity of 1953 mAh g^{-1} and 1273 mAh g^{-1}, respectively. The rate performance of Si^{Cu} prepared via the solution method was also briefly examined. Fig. 8b displays the specific capacities of Si^{Cu} with 1%, 2% and 5% Cu at different C-rates following 3 formation steps at C/10. As illustrated in Fig. 8b, the specific capacities increase with higher Cu content. The specific capacities for the 1% and 2% systems are similar, whereas the Si with 5% Cu

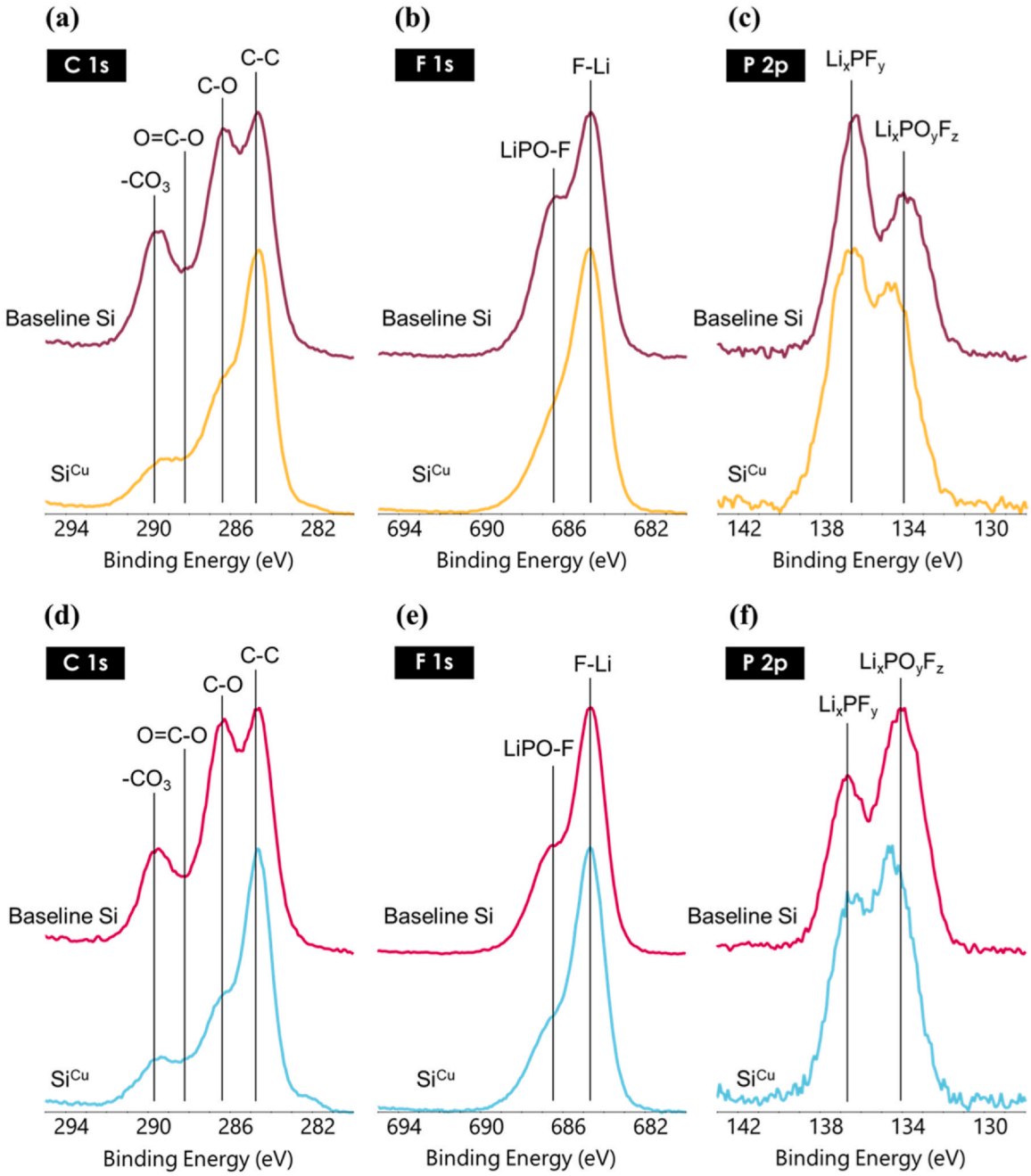

Fig. 6. XPS (a) carbon 1 s, (b) fluorine 1 s, and (c) phosphorous 2p spectra of the baseline Si and Si^{Cu} (milled) after the first delithiation with 80:10:10 mass ratio for Si:binder:conductive additive and (d) carbon 1 s, (e) fluorine 1 s, and (f) phosphorous 2p spectra of the baseline Si and Si^{Cu} (milled) after the first delithiation with 85:10:5 composition for Si:binder:conductive additive.

delivers approximately 300 mAh g^{-1} more capacity from C/3–1C. Additionally, the 5% system maintains its capacity above 2000 mAh g^{-1} at 2C, whereas the other 2 materials drop below 2000 mAh g^{-1} during cycling at 2C. Upon reduction of the C-rate to C/5, the specific capacities are accompanied by a steep capacity loss.

Compared with the milled Si^{Cu}, the solution-prepared systems generally deliver more capacity, which could be attributed to either the synthesis method employed or the wider voltage window used for cycling, that is, 10 mV to 1.5 V, as opposed to 50 mV to 1 V for the milled Si^{Cu}. However, the sol–gel-grown Si^{Cu} seems to undergo some deleterious processes, which prevent the electrode from returning to the capacity initially observed at C/5. By contrast, the milled samples seem to exhibit better capacity retention when returned to lower C-rates. For better comparison, a baseline Si was fabricated and cycled in the 10 mV to 1.5 V voltage window and compared against the solution-prepared Si^{Cu}. The homogeneously dispersed Cu, as seen from STEM characterization, mimics the effect of the PVD-grown Si^{Cu}, which effectively blocks the surface of the electrode, limiting the rate performance of the resulting materials (Fig. S11a). Further, there is no change in the overvoltage of the cells with the sol–gel-grown Si^{Cu} (Fig. S11b–c).

To evaluate the influence of Cu on leakage current, often associated with parasitic reactions, Si^{Cu} electrodes were coupled with NMC811 cathodes, and the current was monitored over time in the charged state after formation cycles. Fig. 8c shows that the Si^{Cu} electrodes exhibit lower leakage currents compared with the baseline material, indicating that the presence of Cu can inhibit parasitic side reactions. This finding reinforces the potential of Cu as a substitute for C, which was previously found to contribute to leakage currents and promote electrolyte

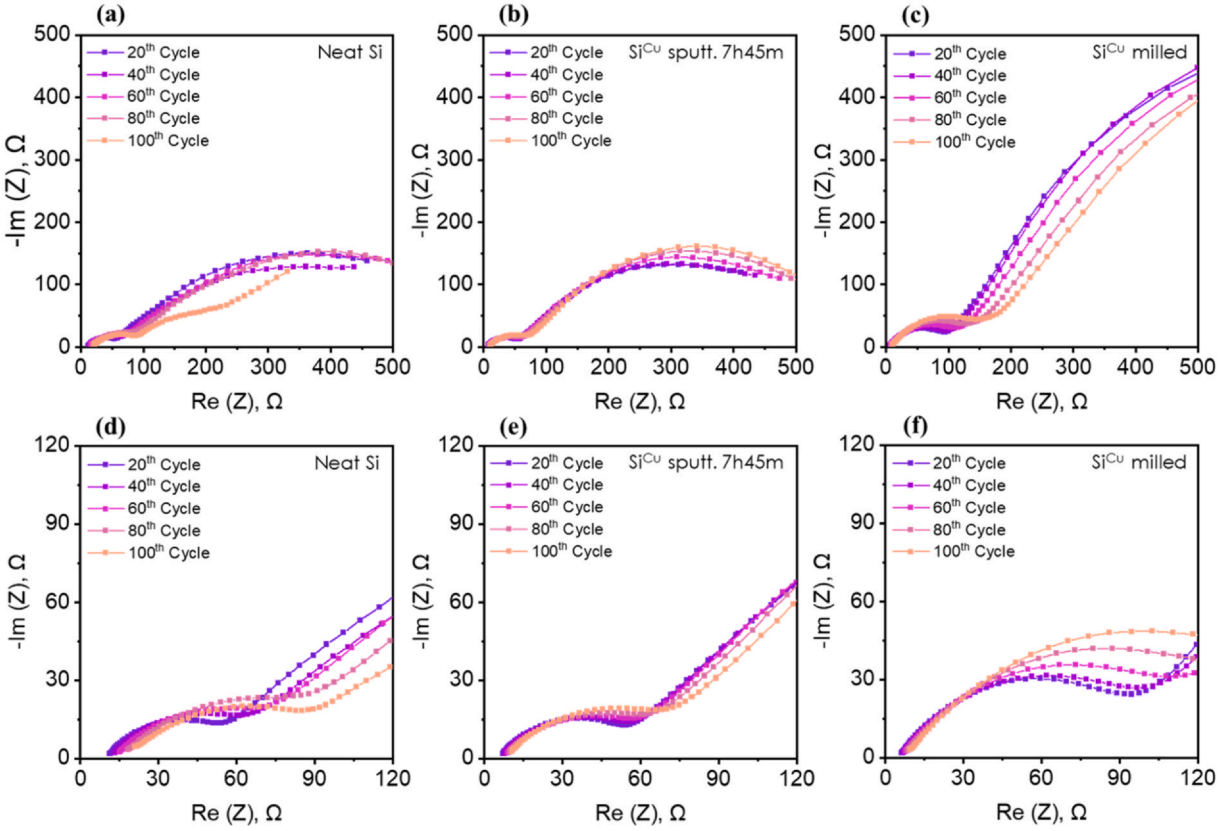

Fig. 7. Nyquist plots at delithiated states of the cells with the (a) baseline Si and (b) Si^{Cu} (sputtered 7 h 45 m), and (c) Si^{Cu} (milled) and (d–f) the same cells with the Nyquist plots focusing on the first semicircle region.

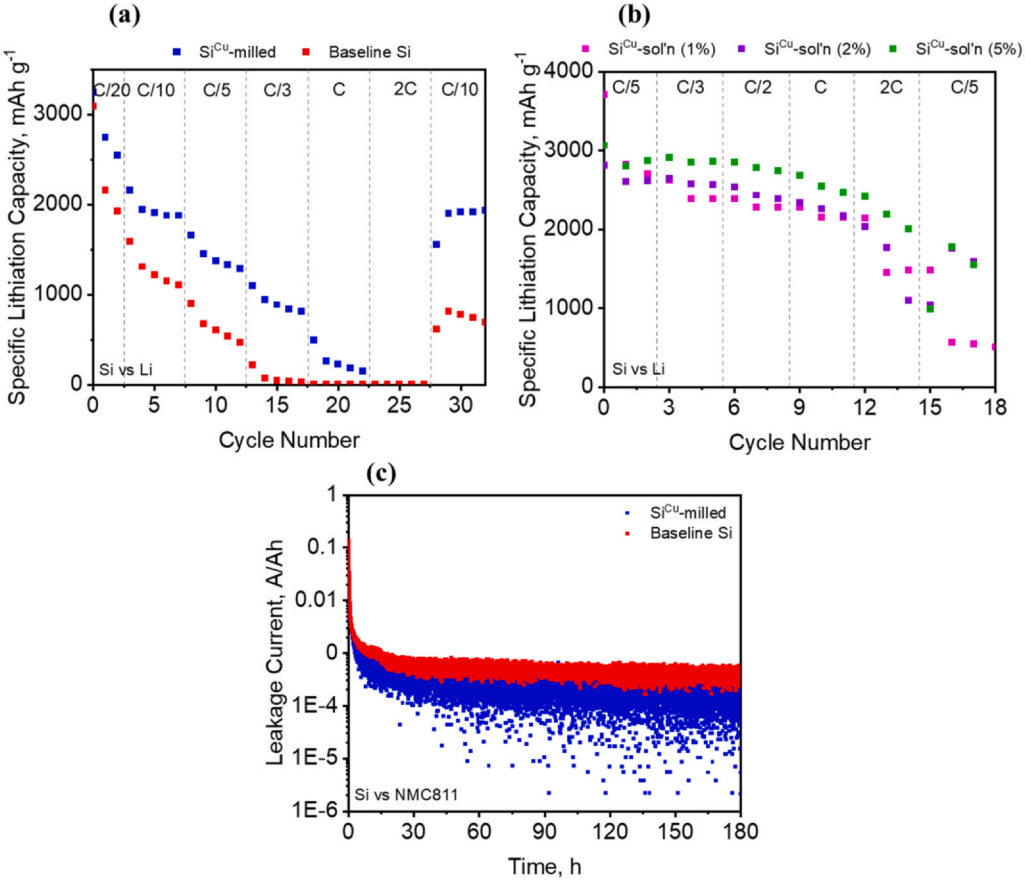

Fig. 8. a) Half-cell rate performance of the baseline Si and milled Si^{Cu} cycled between 50 mV and 1 V, (b) half-cell rate performance of solution-prepared Si^{Cu} cycled between 10 mV and 1.5 V in Gen 2 + 3 wt% FEC electrolyte at room temperature and (c) leakage current in Si–NMC811 full cells at 4.1 V as a function of voltage hold time.

decomposition. However, optimizing the Cu concentration is necessary because reducing the carbon content leads to lower specific capacities that are likely due to lower electronic percolation.

The above data highlight that the mechanochemical formation of Si^{Cu} materials results in a material with unique properties, including faster charge-transfer performance, lower interfacial resistance, and lower overvoltages with cycling. This improvement occurs on samples with clearly heterogeneous distribution of the Cu ad-species and is not a uniform surface coating. Interestingly, the growth of purely metallic Cu particles from PVD or solution precipitation/reduction did not have a positive effect on the resulting materials' performance. While the exact origin of this effect is unclear, there are key indications of the origin of these performance improvements. First, the mechanochemical formed Si^{Cu} had a mixture of metallic and Cu^{1+} species in the XPS (Fig. 2 and S4). While it is not expected that the Cu^{1+} would remain oxidized during lithiation it is *hypothesized* that the presence of mixtures of Cu^0 and Cu^{1+} changed the reaction pathways on the surface resulting in a different SEI composition and the resulting ion transport evidenced in the EIS work (Fig. 7). The resulting surface may facilitate ion desolvation/solvation during charge/discharge resulting in the faster ion transport observed in the cycling data (Fig. 5). Further, the Cu on the surface changes the electrical resistivity of the cell (as evidenced by the SSRM data in Fig. 4) facilitating electron transport during cycling. This change in interface also promotes the formation of a different, potentially more stable SEI, due to accelerated $LiPF_6$ decomposition (Fig. 6). We hypothesize that the heteroatom distribution promotes electron transfer between particles through point contacts. Second, the Cu heteroclusters promote desolvation and the resulting transport of Li atoms on the surface of the Si. Too uniform a coating blocks this desolvation-promoting effect by blocking points for Li to enter into the Si. Should this interpretation of the data be correct, it points to a pathway to improve interfacial properties beyond traditional electrolyte modifications.

4. Conclusion

In conclusion, Cu decoration on Si particles presents a promising avenue for enhancing the performance of Li-ion batteries. Mechanochemical milling and PVD techniques were used to achieve distinct architectures of Si particles decorated with Cu. The high-energy ball-milling approach resulted in island-like features of Cu on the Si surface, whereas PVD provided controlled deposition thickness. Analysis via various techniques revealed differences in particle sizes, crystallinity, resistivity, and surface characteristics such as zeta potential and oxidation state between milled and sputtered samples. Despite changes in physicochemical properties, both approaches demonstrated uniform distribution within the electrode, crucial for enhancing electronic conductivity. Electrochemical investigation showcased improved cycling stability and rate performance achieved using the milled Si^{Cu} electrodes compared with baseline Si. This result is attributed to the significantly lower overpotential of Si^{Cu}, which is likely due to its enhanced conductivity and the nature of the SEI formed during cycling. Moreover, the superior cycling stability of the milled Si^{Cu} compared with sputtered Si^{Cu} is ascribed to a more stable Cu deposit on Si, as evidenced by the formation of Cu_3Si alloy. Importantly, we have also demonstrated lower parasitic currents with Si^{Cu} cells compared with the baseline electrode, supporting the potential of Cu in replacing carbon. However, challenges remain regarding the reduction or complete elimination of carbon while maintaining electrode conductivity. While Cu is not the most economically feasible coating material, the results demonstrate the ability to tune interface resistances, accelerate transport, and reduce overvoltages during cycling. Our findings suggest that further optimization of Cu concentration is necessary to achieve this goal. So far, the solution-prepared Si^{Cu} particles demonstrate that increasing Cu concentration correlates with higher specific capacities. However, an excessive amount of Cu on the Si surface can impede Li^+ ion transport, as suggested by the results from the PVD-grown particles. Overall, this study highlights the potential of metal decoration via high-energy milling as a viable strategy for enhancing the cycling and calendar life of Si electrodes in Li-ion batteries.

Declaration of Competing Interest

The authors declare the following financial interests/personal relationships which may be considered as potential competing interests. Khryslyn G. Arano has patent #63/606,165 pending to UT-Battelle. Gabriel M. Veith has patent #63/606,165 pending to UT-Battelle. Beth L. Armstrong has patent #63/606,165 pending to UT-Battelle. If there are other authors, they declare that they have no known competing financial interests or personal relationships that could have appeared to influence the work reported in this paper.

Acknowledgments

This research was supported by the US Department of Energy, Vehicle Technologies Office (DOE-VTO) under the Silicon Consortium Project, directed by Nicolas Eidson, Carine Steinway, Thomas Do, and Brian Cunningham, and managed by Anthony Burrell. This manuscript has been authored in part by UT-Battelle, LLC, under contract DE-AC05-00OR22725 with DOE. The publisher, by accepting the article for publication, acknowledges that the US government retains a non-exclusive, paid-up, irrevocable, worldwide license to publish or reproduce the published form of this manuscript, or allow others to do so, for US government purposes. DOE will provide public access to these results of federally sponsored research in accordance with the DOE Public Access Plan (http://energy.gov/downloads/doepublic-accessplan). The STEM characterization work was conducted in the William R. Wiley Environmental Molecular Sciences Laboratory, a national scientific user facility sponsored by DOE's Office of Biological and Environmental Research and located at Pacific Northwest National Laboratory, which is operated by Battelle for DOE under Contract DE-AC05-76RL01830. STEM-EDS work was performed in part at the Analytical Instrumentation Facility (AIF) at North Carolina State University, which is supported by the State of North Carolina and the National Science Foundation (award number ECCS-2025064). The AIF is a member of the North Carolina Research Triangle Nanotechnology Network, a site in the National Nanotechnology Coordinately Infrastructure.

Appendix A. Supporting information

Supplementary data associated with this article can be found in the online version at doi:10.1016/j.nxener.2025.100335.

References

[1] M.N. Obrovac, L.J. Krause, Reversible cycling of crystalline silicon powder, J. Electrochem. Soc. 154 (2) (2007) A103–A108, https://doi.org/10.1149/1.2402112.
[2] Y. Lu, Z. Ye, Y. Zhao, Q. Li, M. He, C. Bai, X. Wang, Y. Han, X. Wan, S. Zhang, Y. Ma, Y. Chen, Graphene supported double-layer carbon encapsulated silicon for high-performance lithium-ion battery anode materials, Carbon 201 (2023) 962–971, https://doi.org/10.1016/j.carbon.2022.10.010.
[3] L. Sun, X. Wang, Y. Liu, H. Xu, H. Wang, Y. Lu, Z. Jin, Facile redox synthesis and surface engineering of porous silicon from Zintl compound for high-performance lithium ion battery anodes, ACS Appl. Mater. Interfaces 16 (39) (2024) 52349–52357, https://doi.org/10.1021/acsami.4c10691.
[4] L. Sun, Y. Liu, L. Wang, Z. Chen, Z. Jin, Stabilizing porous micro-sized silicon anodes via construction of tough composite interface networks for high-energy-density lithium-ion batteries, Nano Res. (2024).
[5] L. Sun, Y. Liu, L. Wang, Z. Jin, Advances and future prospects of micro-silicon anodes for high-energy-density lithium-ion batteries: a comprehensive review, Adv. Funct. Mater. 34 (39) (2024) 2403032, https://doi.org/10.1002/adfm.202403032.
[6] K.G. Araño, B.L. Armstrong, G. Yang, C. Kumara, T.Z. Ward, H.M. Meyer, A.M. Rogers, E. Toups, G.M. Veith, Elucidating the role of carbon conductive additive in the processing and electrochemical behavior of surface-modified Si anodes, Energy Fuels 38 (7) (2024) 6446–6458, https://doi.org/10.1021/acs.energyfuels.4c00039.

[7] L. Fransson, T. Eriksson, K. Edström, T. Gustafsson, J.O. Thomas, Influence of carbon black and binder on Li-ion batteries, J. Power Sources 101 (1) (2001) 1–9, https://doi.org/10.1016/S0378-7753(01)00481-5.

[8] D. Molina Piper, S.B. Son, J.J. Travis, Y. Lee, S.S. Han, S.C. Kim, K.H. Oh, S.M. George, S.H. Lee, C. Ban, Mitigating irreversible capacity losses from carbon agents via surface modification, J. Power Sources 275 (2015) 605–611, https://doi.org/10.1016/j.jpowsour.2014.11.032.

[9] D.H.S. Tan, Y.T. Chen, H. Yang, W. Bao, B. Sreenarayanan, J.M. Doux, W. Li, B. Lu, S.Y. Ham, B. Sayahpour, J. Scharf, E.A. Wu, G. Deysher, H.E. Han, H.J. Hah, H. Jeong, J.B. Lee, Z. Chen, Y.S. Meng, Carbon-free high-loading silicon anodes enabled by sulfide solid electrolytes, Science 373 (6562) (2021) 1494–1499, https://doi.org/10.1126/science.abg7217.

[10] K.G. Araño, G. Yang, B.L. Armstrong, T. Aytug, M.S. Chambers, E.C. Self, H.M. Meyer, J. Quinn, J.F. Browning, C. Wang, G.M. Veith, Carbon coating influence on the formation of percolating electrode networks for silicon anodes, ACS Appl. Energy Mater. 6 (21) (2023) 11308–11321, https://doi.org/10.1021/acsaem.3c02205.

[11] M.N. Obrovac, V.L. Chevrier, Alloy negative electrodes for Li-ion batteries, Chem. Rev. 114 (23) (2014) 11444–11502, https://doi.org/10.1021/cr500207g.

[12] J.W. Kim, J.H. Ryu, K.T. Lee, S.M. Oh, Improvement of silicon powder negative electrodes by copper electroless deposition for lithium secondary batteries, J. Power Sources 147 (1–2) (2005) 227–233, https://doi.org/10.1016/j.jpowsour.2004.12.041.

[13] X. Yang, Z. Wen, S. Huang, X. Zhu, X. Zhang, Electrochemical performances of silicon electrode with silver additives, Solid State Ion. 177 (26-32 SPEC. ISS.) (2006) 2807–2810, https://doi.org/10.1016/j.ssi.2006.03.033.

[14] Y. Yu, L. Gu, C. Zhu, S. Tsukimoto, P.A. Van Aken, J. Maier, Reversible storage of lithium in silver-coated three-dimensional macroporous silicon, Adv. Mater. 22 (20) (2010) 2247–2250, https://doi.org/10.1002/adma.200903755.

[15] D. Chen, X. Mei, G. Ji, M. Lu, J. Xie, J. Lu, J.Y. Lee, Reversible lithium-ion storage in silver-treated nanoscale hollow porous silicon particles, Angew. Chem. - Int. Ed. 51 (10) (2012) 2409–2413, https://doi.org/10.1002/anie.201107885.

[16] S. Murugesan, J.T. Harris, B.A. Korgel, K.J. Stevenson, Copper-coated amorphous silicon particles as an anode material for lithium-ion batteries, Chem. Mater. 24 (7) (2012) 1306–1315, https://doi.org/10.1021/cm2037475.

[17] B.D. Polat, O. Keles, Improving Si anode performance by forming copper capped copper-silicon thin film anodes for rechargeable lithium ion batteries, Electrochim. Acta 170 (2015) 63–71, https://doi.org/10.1016/j.electacta.2015.04.131.

[18] S. Yoo, J.I. Lee, S. Ko, S. Park, Highly dispersive and electrically conductive silver-coated si anodes synthesized via a simple chemical reduction process, Nano Energy 2 (6) (2013) 1271–1278, https://doi.org/10.1016/j.nanoen.2013.06.006.

[19] H. Zhang, S. Liu, X. Yu, S. Chen, Improving rate capacity and cycling stability of Si-anode lithium ion battery by using copper nanowire as conductive additive, J. Alloy. Compd. 822 (2020) 153664, https://doi.org/10.1016/j.jallcom.2020.153664.

[20] S.H. Moon, S.J. Kim, M.C. Kim, J.Y. So, J.E. Lee, Y.K. Shin, W.G. Bae, K.W. Park, Stress-relieved Si anode on a porous Cu current collector for high-performance lithium-ion batteries, June 2018, Mater. Chem. Phys. 223 (2019) 152–156, https://doi.org/10.1016/j.matchemphys.2018.10.042.

[21] K. Guo, Q. Pan, L. Wang, S. Fang, Nano-scale copper-coated graphite as anode material for lithium-ion batteries, J. Appl. Electrochem. 32 (6) (2002) 679–685, https://doi.org/10.1023/A:1020178121795.

[22] I. Sandu, T. Brousse, D.M. Schleich, Effect of nickel coating on electrochemical performance of graphite anodes for lithium ion batteries, Ionics 9 (5–6) (2003) 329–335, https://doi.org/10.1007/BF02376582.

[23] L.J. Fu, J. Gao, T. Zhang, Q. Cao, L.C. Yang, Y.P. Wu, R. Holze, Effect of Cu2O coating on graphite as anode material of lithium ion battery in PC-based electrolyte, J. Power Sources 171 (2) (2007) 904–907, https://doi.org/10.1016/j.jpowsour.2007.05.099.

[24] J. Yun, Y. Wang, T. Gao, H. Zheng, M. Shen, Q. Qu, H. Zheng, In-situ electrochemical coating of Ag nanoparticles onto graphite electrode with enhanced performance for Li-ion batteries, Electrochim. Acta 155 (2015) 396–401, https://doi.org/10.1016/j.electacta.2014.12.129.

[25] K.G. Araño, B.L. Armstrong, E. Boeding, G. Yang, H.M. Meyer, E. Wang, R. Korkosz, K.L. Browning, T. Malkowski, B. Key, G.M. Veith, Functionalized silicon particles for enhanced half- and full-cell cycling of Si-based Li-ion batteries, ACS Appl. Mater. Interfaces 15 (8) (2023) 10554–10569, https://doi.org/10.1021/acsami.2c16978.

[26] J. Cai, X. Zhou, T. Li, H.T. Nguyen, G.M. Veith, Y. Qin, W. Lu, S.E. Trask, M.T. Fonseca Rodrigues, Y. Liu, W. Xu, M.C. Schulze, A.K. Burrell, Z. Chen, Critical contribution of imbalanced charge loss to performance deterioration of Si-based lithium-ion cells during calendar aging, ACS Appl. Mater. Interfaces 15 (41) (2023) 48085–48095, https://doi.org/10.1021/acsami.3c08015.

[27] G.M. Veith, A.R. Lupini, S.J. Pennycook, G.W. Ownby, N.J. Dudney, Nanoparticles of gold on γ-Al2O3 produced by Dc magnetron sputtering, J. Catal. 231 (1) (2005) 151–158, https://doi.org/10.1016/j.jcat.2004.12.008.

[28] G.M. Veith, A.R. Lupini, S.J. Pennycook, N.J. Dudney, Influence of support hydroxides on the catalytic activity of oxidized gold clusters, ChemCatChem 2 (3) (2010) 281–286, https://doi.org/10.1002/cctc.200900243.

[29] Y. Kim, N.J. Dudney, M. Chi, S.K. Martha, J. Nanda, G.M. Veith, C. Liang, A perspective on coatings to stabilize high-voltage cathodes: LiMn 1.5 Ni 0.5 O 4 with sub-nanometer lipon cycled with LiPF 6 electrolyte, J. Electrochem. Soc. 160 (5) (2013) A3113–A3125, https://doi.org/10.1149/2.017305jes.

[30] G.M. Veith, A.R. Lupini, L. Baggetto, J.F. Browning, J.K. Keum, A. Villa, L. Prati, A.B. Papandrew, G.A. Goenaga, D.R. Mullins, S.E. Bullock, N.J. Dudney, Evidence for the formation of nitrogen-rich platinum and palladium nitride nanoparticles, Chem. Mater. 25 (24) (2013) 4936–4945, https://doi.org/10.1021/cm403224m.

[31] Y. Rakita, D. O'Nolan, R.D. McAuliffe, G.M. Veith, P.J. Chupas, S.J.L. Billinge, K.W. Chapman, Active reaction control of Cu redox state based on real-time feedback from in situ synchrotron measurements, J. Am. Chem. Soc. 142 (44) (2020) 18758–18762, https://doi.org/10.1021/jacs.0c09418.

[32] G.M. Veith, A.R. Lupini, N.J. Dudney, Role of PH in the formation of structurally stable and catalytically active TiO 2-supported gold catalysts, J. Phys. Chem. C. 113 (1) (2009) 269–280, https://doi.org/10.1021/jp808249f.

[33] H.M. Rietveld, A profile refinement method for nuclear and magnetic structures, J. Appl. Crystallogr. 2 (2) (1969) 65–71, https://doi.org/10.1107/S0021889869006558.

[34] A.A. Coelho, J. Evans, I. Evans, A. Kern, S. Parsons, The TOPAS symbolic computation system, Powder Diffr. 26 (S1) (2011) S22–S25, https://doi.org/10.1154/1.3661087.

[35] D.M. Többens, N. Stüßer, K. Knorr, H.M. Mayer, G. Lampert, E9: the new high-resolution neutron powder diffractometer at the berlin neutron scattering center (Trans Tech Publications Ltd), Eur. Powder Diffr. EPDIC 7; Mater. Sci. Forum 378 (2001) 288–293, https://doi.org/10.4028/www.scientific.net/MSF.378-381.288.

[36] E.G. Shkvarina, A.A. Titov, A.S. Shkvarin, J.R. Plaisier, L. Gigli, A.N. Titov, Thermal stability of the layered modification of Cu0.5ZrTe2 in the temperature range 25–900 °C, Acta Crystallogr. Sect. C 74 (9) (2018) 1020–1025, https://doi.org/10.1107/S2053229618009841.

[37] M.L. Foo, Q. Huang, J.W. Lynn, W.L. Lee, T. Klimczuk, I.S. Hagemann, N.P. Ong, R.J. Cava, Synthesis, structure and physical properties of Ru ferrites: BaMRu 5O11 (M = Li and Cu) and BaM′2Ru 4O11 (M′ = Mn, Fe and Co), J. Solid State Chem. 179 (2) (2006) 563–572, https://doi.org/10.1016/j.jssc.2005.11.014.

[38] E. Dodony, G.Z. Radnóczi, I. Dódony, Low temperature formation of copper rich silicides, Intermetallics 107 (January) (2019) 108–115, https://doi.org/10.1016/j.intermet.2019.01.010.

[39] D. Balzar, N. Audebrand, M.R. Daymond, A. Fitch, A. Hewat, J.I. Langford, A. Le Bail, D. Louër, O. Masson, C.N. McCowan, N.C. Popa, P.W. Stephens, B.H. Toby, Size-strain line-broadening analysis of the ceria round-robin sample, J. Appl. Crystallogr 37 (6) (2004) 911–924, https://doi.org/10.1107/S0021889804022551.

[40] P. Eyben, M. Xu, N. Duhayon, T. Clarysse, S. Callewaert, W. Vandervorst, Scanning spreading resistance microscopy and spectroscopy for routine and quantitative two-dimensional carrier profiling, J. Vac. Sci. Technol. B Microelectron. Nanom. Struct. Process. Meas. Phenom. 20 (1) (2002) 471–478, https://doi.org/10.1116/1.1424280.

[41] P. Eyben, F. Clemente, K. Vanstreels, G. Pourtois, T. Clarysse, E. Duriau, T. Hantschel, K. Sankaran, J. Mody, W. Vandervorst, K. Mylvaganam, L. Zhang, Analysis and modeling of the high vacuum scanning spreading resistance microscopy nanocontact on silicon, J. Vac. Sci. Technol. B 28 (2) (2010) 401–406, https://doi.org/10.1116/1.3273895.

[42] L.H. Wang, S. Gao, L.L. Ren, E.L. Zhou, Y.F. Qin, The synergetic effect induced high electrochemical performance of CuO/Cu2O/Cu nanocomposites as lithium-ion battery anodes (November 2021), Front. Chem. 9 (2021) 1–9, https://doi.org/10.3389/fchem.2021.790659.

[43] H. Adenusi, G.A. Chass, S. Passerini, K.V. Tian, G. Chen, Lithium batteries and the solid electrolyte interphase (SEI)—progress and outlook, Adv. Energy Mater. 13 (10) (2023), https://doi.org/10.1002/aenm.202203307.

[44] L.A. Berla, S.W. Lee, I. Ryu, Y. Cui, W.D. Nix, Robustness of amorphous silicon during the initial lithiation/delithiation cycle, J. Power Sources 258 (2014) 253–259, https://doi.org/10.1016/j.jpowsour.2014.02.032.

[45] M.T. McDowell, S.W. Lee, J.T. Harris, B.A. Korgel, C. Wang, W.D. Nix, Y. Cui, In situ TEM of two-phase lithiation of amorphous silicon nanospheres, Nano Lett. 13 (2) (2013) 758–764, https://doi.org/10.1021/nl3044508.

[46] S. Chen, A. Du, C. Yan, Molecular dynamic investigation of the structure and stress in crystalline and amorphous silicon during lithiation, Comput. Mater. Sci. 183 (February) (2020) 109811, https://doi.org/10.1016/j.commatsci.2020.109811.

[47] A. Ulvestad, A.H. Reksten, H.F. Andersen, P.A. Carvalho, I.J.T. Jensen, M.U. Nagell, J.P. Mæhlen, M. Kirkengen, A.Y. Koposov, Crystallinity of silicon nanoparticles: direct influence on the electrochemical performance of lithium ion battery anodes, ChemElectroChem 7 (21) (2020) 4349–4353, https://doi.org/10.1002/celc.202001108.

[48] T.R. Jow, M.B. Marx, J.L. Allen, Distinguishing Li+ charge transfer kinetics at NCA/electrolyte and graphite/electrolyte interfaces, and NCA/electrolyte and LFP/electrolyte interfaces in Li-ion cells, J. Electrochem. Soc. 159 (5) (2012) A604, https://doi.org/10.1149/2.079205jes.

[49] M. Oldenburger, B. Bedürftig, A. Gruhle, F. Grimsmann, E. Richter, R. Findeisen, A. Hintennach, Investigation of the low frequency Warburg impedance of Li-ion cells by frequency domain measurements, J. Energy Storage 21 (June 2018) (2019) 272–280, https://doi.org/10.1016/j.est.2018.11.029.

[50] A. Lasia, Electrochemical impedance spectroscopy and its applications, Springer New York, New York, NY, 2014, https://doi.org/10.1007/978-1-4614-8933-7.